processes

MDPI

Article

The Multi-Objective Distributed Robust Optimization Scheduling of Integrated Energy Systems Considering Green Hydrogen Certificates and Low-Carbon Demand Response

Yulong Yang, Han Yan * and Jiaqi Wang

School of Electrical Engineering, Northeast Electric Power University, Jilin 132000, China; yangyulong@neepu.edu.cn (Y.Y.); 2202200180@neepu.edu.cn (J.W.)
* Correspondence: 2202200346@neepu.edu.cn

Abstract: To address the issues of energy wastage and uncertainty impacts associated with high levels of renewable energy integration, a multi-objective distributed robust low-carbon optimization scheduling strategy for hydrogen-integrated Integrated Energy Systems (IES) is proposed. This strategy incorporates a green hydrogen trading mechanism and low-carbon demand response. Firstly, to leverage the low-carbon and clean characteristics of hydrogen energy, an efficient hydrogen utilization model was constructed, consisting of electricity-based hydrogen production, waste heat recovery, multi-stage hydrogen use, hydrogen blending in gas, and hydrogen storage. This significantly enhanced the system's renewable energy consumption and carbon reduction. Secondly, to improve the consumption of green hydrogen, a novel reward–punishment green hydrogen certificate trading mechanism was proposed. The impact of green hydrogen trading prices on system operation was discussed, promoting the synergistic operation of green hydrogen and green electricity. Based on the traditional demand-response model, a novel low-carbon demand-response strategy is proposed, with carbon emission factors serving as guiding signals. Finally, considering the uncertainty of renewable energy, an innovative optimal trade-off multi-objective distributed robust model was proposed, which simultaneously considered low-carbon, economic, and robustness aspects. The model was solved using an improved adaptive particle swarm optimization algorithm. Case study results show that, after introducing the reward–punishment green hydrogen trading mechanism and low-carbon demand response, the system's total cost was reduced by approximately 5.16% and 4.37%, and carbon emissions were reduced by approximately 7.84% and 6.72%, respectively. Moreover, the proposed multi-objective distributed robust model not only considers the system's economy, low-carbon, and robustness but also offers higher solving efficiency and optimization performance compared to multi-objective optimization methods.

Keywords: green hydrogen certificate trading; low carbon demand response; distributed robustness; integrated energy system; optimization scheduling

check for updates

Academic Editor: Paola Ammendola

Received: 20 January 2025
Revised: 24 February 2025
Accepted: 25 February 2025
Published: 28 February 2025

Citation: Yang, Y.; Yan, H.; Wang, J. The Multi-Objective Distributed Robust Optimization Scheduling of Integrated Energy Systems Considering Green Hydrogen Certificates and Low-Carbon Demand Response. *Processes* **2025**, *13*, 703. https://doi.org/10.3390/pr13030703

Copyright: © 2025 by the authors. Licensee MDPI, Basel, Switzerland. This article is an open access article distributed under the terms and conditions of the Creative Commons Attribution (CC BY) license (https://creativecommons.org/licenses/by/4.0/).

1. Introduction

With the rapid increase in installed capacity of renewable energy, its volatility, intermittency, and integration issues will impact its broader development [1,2]. Hydrogen energy, a secondary clean energy with high energy density that is easy to store and transport, can effectively facilitate the integration of renewable energy and reduce energy wastage [3]. Based on different hydrogen production sources, hydrogen can be classified into green hydrogen, blue hydrogen, and gray hydrogen, among which green hydrogen can effectively

reduce carbon emissions in the hydrogen energy industry chain and play an important role in achieving carbon neutrality goals [4].

As the low-carbon and high-efficiency characteristics of hydrogen energy become more prominent, scholars both domestically and internationally have conducted in-depth research on its application in Integrated Energy Systems (IES). Reference [5] introduced a two-stage conversion process of hydrogen energy, including electricity-to-hydrogen, hydrogen-to-electricity, and hydrogen-to-methane, into the IES framework, realizing the coupling conversion of electricity, heat, hydrogen, and gas. Reference [6] proposed a low-carbon operation model of hydrogen-based IES with refined hydrogen energy utilization as a medium, incorporated the use of waste heat during hydrogen production and conversion, and verified the multifaceted benefits of the hydrogen utilization model. Reference [7] presented an IES low-carbon economic scheduling model for parks, integrating refined hydrogen utilization, demand response, and a tiered carbon trading mechanism. The study explored a refined hydrogen model and expanded its hydrogen application scenarios. Reference [8] proposed a low-carbon optimization operation strategy for IES with offshore wind power-based hydrogen production, studying the mechanisms of offshore wind hydrogen production and hydrogen transmission. The aforementioned literature mainly focused on hydrogen production and utilization pathways and did not analyze the quality of the hydrogen energy.

The green hydrogen certificate trading (GHCT) mechanism plays a crucial role in promoting new energy-based hydrogen production, exploring the clean characteristics of hydrogen, and reducing carbon emissions. In this regard, Reference [9] defined a green hydrogen certificate based on the green certificate trading mechanism and proposed a green hydrogen certificate trading mechanism based on non-shared and shared benefits. Reference [10] proposed a green hydrogen certificate trading model based on auction principles, increasing the share of hydroelectric hydrogen production. Reference [11] proposed an opportunity-constrained optimization scheduling strategy for electricity-hydrogen IES, considering hydrogen green certificates. It explored the value of green hydrogen in the system and enabled its large-scale utilization. Reference [12] proposed a low-carbon economic dispatch model for IES that considered the GHCT mechanism and carbon quotas for new energy vehicles, promoting the synergistic operation of green electricity and green hydrogen in the system.

Demand-side resources can not only optimize the load curve but also improve the integration of renewable energy and the economic operation of the system, offering multiple benefits. Reference [13] developed an IES scheduling model that incorporated a reward–punishment tiered carbon trading mechanism and the synergistic effect of integrated demand response (IDR) on the demand side, enhancing the regulation and response capacity of the demand side. Reference [14] proposed a multi-type IDR model incorporating price, incentives, and substitution, effectively enhancing the response capacity of demand-side resources. Reference [15] explored the response and regulation capabilities of demand-side resources across different time scales and proposed an IES scheduling model with multi-time-scale IDR, demonstrating the effectiveness of IDR strategies in stabilizing system power fluctuations. Reference [16] considered the uncertainty of user random response behavior in IDR, established an uncertain probability interval for IDR, and proposed a two-stage stochastic optimization strategy for IES, considering demand-side uncertainty. Most of the above studies analyzed the response capability of demand-side IDR from the perspective of "television angle", while References [17,18] proposed a low-carbon demand response (LCDR) model based on the low-carbon characteristics of the demand response to guide low-carbon dispatch on the supply side. However, they did not explore the

synergistic effects between the low-carbon demand-response model, source-side hydrogen utilization, and the green hydrogen certificate trading mechanism.

As the installed capacity of renewable energy increases, its intermittency, volatility, and other uncertainties have a significant impact on the stable operation of IES or power systems. Currently, stochastic programming [19] and robust optimization [20] are primarily used to address source and load uncertainties in IES. To address source and load uncertainties in the system, Reference [21] proposed a multi-objective optimization scheduling model based on stochastic programming theory, aiming to maximize profits. Reference [22] proposed a two-stage robust optimization scheduling framework that combined energy recovery, demand response, and forecasting for optimizing microgrid scheduling, balancing the system economy and robustness. Reference [23] proposed an improved distributed robust optimization scheduling method to address issues of under- or over-adjustment caused by energy prediction uncertainties, enhancing the system robustness. Reference [24] proposed a distributed robust low-carbon scheduling strategy for IES, considering source-load collaborative carbon reduction, and constructed a data-driven distributed robust optimization model. Reference [25] focused on the uncertainty of renewable energy and prices, proposing a robust optimization scheduling strategy for IES that considers price uncertainty. It demonstrated the specific impact of market price fluctuations on system operation.

However, despite the extensive research on IDR strategies, hydrogen utilization, and IES robust optimization in existing studies, there are still the following shortcomings:

(1) There is still limited research on the application of the GHCT mechanism in IES, and the synergistic effect between the GHCT mechanism and demand-side response has not been thoroughly analyzed, nor has the impact of green hydrogen trading prices on IES operational optimization been investigated.
(2) Most current studies analyzed the response capability of demand-side IDR from the perspective of electricity, without exploring the synergistic effects among low-carbon demand-response models, source-side hydrogen utilization, and green hydrogen certificate trading mechanisms.
(3) Most current literature on IES robust optimization methods only considered the system's economic performance, with robustness being arbitrarily set, which introduces significant subjective limitations. Furthermore, multiple system indicators, such as low-carbon, economic performance, and robustness, were not simultaneously considered in the optimization process.

To address the above issues, this paper comprehensively considered the system's low-carbon performance, economy, and robustness, and proposed a multi-objective distributed robust optimization scheduling strategy for IES that incorporates green hydrogen trading and low-carbon demand response. The main contributions of this paper are listed as follows:

(1) An efficient hydrogen energy utilization model was constructed, including hydrogen production, hydrogen usage, hydrogen blending with natural gas, and hydrogen storage, while introducing green hydrogen certificates. A green hydrogen certificate trading mechanism was proposed to promote the synergistic operation of green hydrogen and green electricity, thus enhancing the integration of renewable energy.
(2) Demand response was incorporated. Based on the traditional demand-response model, a low-carbon demand-response strategy was proposed, guided by carbon emission factors, to improve the system's economy and low-carbon performance.
(3) Considering the uncertainty of renewable energy, a multi-objective optimization compromise method was proposed based on the ideal solution approximation and multi-objective decision theory, considering low-carbon performance, economy, and robustness. An optimal compromise multi-objective distributed robust model for IES

was constructed, and the proposed model was solved using an improved adaptive particle swarm optimization (IA-PSO) algorithm. This method not only considers the system's low-carbon performance, economy, and robustness simultaneously but also improves the solution efficiency and optimization performance.

The subsequent chapters are arranged as follows: Section 2 discusses the IES framework and modeling for efficient hydrogen energy utilization; Section 3 explains the green hydrogen certificate trading mechanism; Section 4 constructs the low-carbon demand-response model; Section 5 builds the IES chance-constrained distributed robust model; Section 6 conducts comparative analysis through scenario construction to validate the effectiveness and practicality of the model; and Section 7 provides a summary of the research and concludes the study.

2. IES Architecture of Hydrogen Containing Energy

Figure 1 presents the proposed IES framework with hydrogen integration, which includes efficient hydrogen utilization, a combined heat and power (CHP) supply, and multi-energy storage components. The system integrates a large-scale wind farm and photo-voltaic power station to provide clean energy. The efficient hydrogen utilization section includes several stages such as hydrogen production, hydrogen use, hydrogen-doped gas, and hydrogen storage. These stages involve an alkaline electrolyzer (AEL), hydrogen storage tank (HST), hydrogen-doped gas stage, hydrogen fuel cell (HFC), and methane reactor (MR).

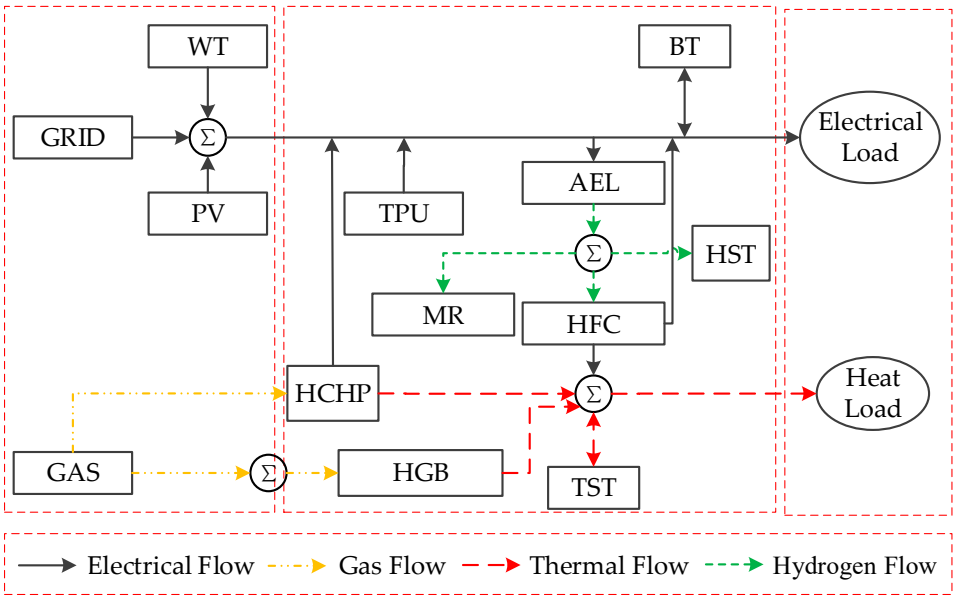


Figure 1. IES architecture for efficient utilization of hydrogen containing energy.

The system includes both electrical and thermal loads. The electrical load is mainly supplied by wind turbines (WT), photovoltaic systems (PV), hydrogen-doped combined heat and power (HCHP), hydrogen fuel cells (HFC), and external power purchase, with energy time-shifting capabilities achieved through batteries (BT). The thermal load is primarily supplied by hydrogen-doped gas boilers (HGB), HFC, and HCHP, with additional support provided by a thermal storage tank (TST).

The efficient hydrogen utilization model consists of five stages: hydrogen production, hydrogen-doped gas, hydrogen-to-heat-and-power conversion, hydrogen-to-methane production, and hydrogen storage. This model can significantly improve wind power integration and reduce wind curtailment. It can be expressed as follows.

2.1. Alkaline Electrolyzer (AEL)

AEL can use electrical energy to split water into hydrogen and oxygen, achieving the system's electricity-to-hydrogen conversion. Traditional EL typically adopts a constant hydrogen production efficiency, which leads to an idealized representation of hydrogen production characteristics. To more accurately reflect the operational characteristics of AEL, a mathematical model for AEL is constructed [7]:

$$\begin{cases} \eta\left[P_t^{\mathrm{AEL,e}}\right] = \alpha_{\mathrm{AEL}}\left(\frac{P_t^{\mathrm{AEL,e}}}{P_{\mathrm{N}}^{\mathrm{AEL,e}}}\right)^2 + \beta_{\mathrm{AEL}}\left(\frac{P_t^{\mathrm{AEL,e}}}{P_{\mathrm{N}}^{\mathrm{AEL,e}}}\right) + \chi_{\mathrm{AEL}} \\ N_t^{\mathrm{H_2}} = \eta\left[P_t^{\mathrm{AEL,e}}\right] R_{\mathrm{N}}^{\mathrm{AEL}} \end{cases} \tag{1}$$

where $P_t^{\mathrm{AEL,e}}$ is the input electrical power to the AEL; $\eta\left[P_t^{\mathrm{AEL,e}}\right]$ is the efficiency function of the AEL; α_{AEL}, β_{AEL} and χ_{AEL} are the coefficients of the AEL's efficiency function; $R_{\mathrm{N}}^{\mathrm{AEL}}$ is the rated capacity of the AEL; $N_t^{\mathrm{H_2}}$ is the amount of hydrogen produced by the AEL; and $P_{\mathrm{N}}^{\mathrm{AEL,e}}$ is the rated value of the AEL's input electrical power.

Since there is heat dissipation during the electrolysis of water, the lost heat can be recovered through waste heat recovery. The hydrogen production power and heat production power of AEL are given by:

$$P_{\mathrm{H_2},t}^{\mathrm{AEL}} = \frac{M_{\mathrm{H_2}} N_t L_{\mathrm{LHV}}^{\mathrm{H}}}{\rho_{\mathrm{H_2}}} \tag{2}$$

$$P_t^{\mathrm{AEL,h}} = \eta_{\mathrm{AEL}}^{\mathrm{h}} P_t^{\mathrm{AEL,e}} \tag{3}$$

where $P_{\mathrm{H_2},t}^{\mathrm{AEL}}$ is the hydrogen production amount of the EL; $\eta_{\mathrm{AEL}}^{\mathrm{h}}$ is the heat recovery efficiency coefficient of the EL; $P_t^{\mathrm{AEL,h}}$ is the recovered waste heat amount of the EL; $\rho_{\mathrm{H_2}}$ is the density of hydrogen; $M_{\mathrm{H_2}}$ is the molar mass of hydrogen; and $L_{\mathrm{LHV}}^{\mathrm{H}}$ is the lower heating value of hydrogen.

2.2. Hydrogen-Doped Gas Turbine Units

Hydrogen doping in natural gas not only further reduces the system's carbon emissions but also diversifies the hydrogen utilization scenarios, promoting hydrogen integration. The hydrogen doping stage can be represented as follows:

$$\begin{cases} g_t^{\mathrm{mix}} = g_t^{\mathrm{H_2}} + g_t^{\mathrm{gas}} \\ \lambda_t^{\mathrm{H}} = g_t^{\mathrm{H_2}} / g_t^{\mathrm{mix}} \\ L_{\mathrm{mix},t}^{\mathrm{LHV}} = \lambda_{\mathrm{H}}^t L_{\mathrm{H}}^{\mathrm{LHV}} + (1 - \lambda_t^{\mathrm{H}}) L_{\mathrm{g}}^{\mathrm{LHV}} \\ 0 \le \lambda_t^{\mathrm{H}} \le 20\% \end{cases} \tag{4}$$

where $g_t^{\mathrm{H_2}}$ and g_t^{gas} are the amounts of hydrogen and natural gas in the natural gas pipeline; g_t^{mix} is the amount of mixed gas in the pipeline; $L_{\mathrm{mix},t}^{\mathrm{LHV}}$ is the heating value of the mixed gas; $L_{\mathrm{H}}^{\mathrm{LHV}}$ and $L_{\mathrm{g}}^{\mathrm{LHV}}$ respectively denote the heating values of hydrogen and natural gas; and λ_t^{H} is the hydrogen doping ratio.

Based on Formula (4), the HCHP model can be represented as follows:

$$\begin{cases} P_{t,\mathrm{e}}^{\mathrm{HCHP}} = \eta_{\mathrm{e}}^{\mathrm{HCHP}} L_{\mathrm{mix},t}^{\mathrm{LHV}} G_t^{\mathrm{HCHP}} \\ P_{t,\mathrm{h}}^{\mathrm{HCHP}} = \eta_{\mathrm{h}}^{\mathrm{HCHP}} L_{\mathrm{mix},t}^{\mathrm{LHV}} G_t^{\mathrm{HCHP}} \end{cases} \tag{5}$$

where G_t^{HCHP} is the input hydrogen-doped gas mixture to the HCHP; $P_{t,\mathrm{e}}^{\mathrm{HCHP}}$ and $P_{t,\mathrm{h}}^{\mathrm{HCHP}}$ respectively denote the output electrical power and thermal power of the HCHP; and

$\eta_{\mathrm{e}}^{\mathrm{HCHP}}$ and $\eta_{\mathrm{h}}^{\mathrm{HCHP}}$, respectively, denote the electrical and thermal conversion efficiencies of the HCHP.

Similarly, the mathematical model for the HGB can be represented as follows:

$$P_{t,\mathrm{h}}^{\mathrm{HGB}} = \eta_{\mathrm{h}}^{\mathrm{HGB}} L_{\mathrm{mix},t}^{\mathrm{LHV}} G_t^{\mathrm{HGB}} \tag{6}$$

where G_t^{HGB} is the input hydrogen-doped gas mixture to the HGB and $P_{t,\mathrm{h}}^{\mathrm{HGB}}$ and $\eta_{\mathrm{h}}^{\mathrm{HGB}}$, respectively, denote the thermal power output and conversion efficiency of the HGB.

2.3. Other Hydrogen Utilization Units

HFC and MR serve as important pathways for hydrogen utilization, converting hydrogen into electricity, heat, and gas. Hydrogen storage tanks allow for the storage of hydrogen, enabling energy time-shifting and realizing the coupling of electricity, heat, gas, and hydrogen. However, since these topics have been extensively discussed in existing literature, further elaboration is not provided here. The mathematical models can be found in references [5–7].

3. Green Hydrogen Certificate Trading (GHCT)

Hydrogen can be classified into gray hydrogen, blue hydrogen, and green hydrogen. Green hydrogen refers to hydrogen produced using renewable energy and has a higher low-carbon characteristic compared to gray and blue hydrogen, serving as a certification of hydrogen quality. Green hydrogen certificate trading (GHCT) refers to a green certificate trading mechanism based on green hydrogen, where the system can obtain a corresponding number of green hydrogen certificates when its use of green hydrogen exceeds the government-set quota. These certificates can then be sold in the hydrogen market to generate revenue. Conversely, if the system uses less than the quota, it must purchase green hydrogen certificates. A schematic diagram of green hydrogen certificate trading is shown in Figure 2.

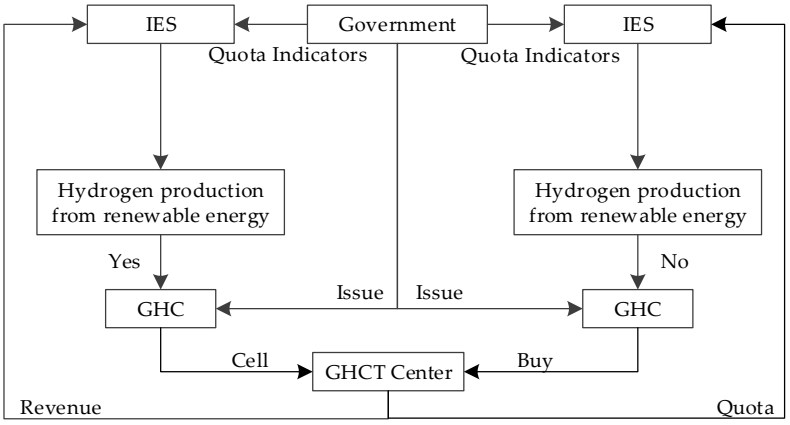


Figure 2. Schematic diagram of green hydrogen trading.

Based on the renewable energy quota system and green certificate trading mechanism, the green hydrogen certificate trading mechanism was constructed and can be represented as follows:

$$Z_{\mathrm{GHCT}} = Z_{\mathrm{IES}} - Z_{\mathrm{new}} \tag{7}$$

$$\begin{cases} Z_{\mathrm{IES}} = \alpha_{\mathrm{gh}} \sum_{t=1}^{T} (P_{t,\mathrm{H_2}}^{\mathrm{HFC}} + P_{t,\mathrm{H_2}}^{\mathrm{MR}} + g_t^{\mathrm{H_2}})/1000 \\ Z_{\mathrm{new}} = \omega_{\mathrm{gh}} \sum_{t=1}^{T} (P_{t,\mathrm{H_2}}^{\mathrm{wind}} + P_{t,\mathrm{H_2}}^{\mathrm{pv}})/1000 \end{cases} \tag{8}$$

where Z_{GHCT} is the number of green hydrogen certificates traded by the IES; Z_{GHCT} and Z_{new} are the green hydrogen certificate quota indicators that the IES must hold and the number of green hydrogen certificates obtained through renewable energy, respectively; $P_{t,\mathrm{H_2}}^{\mathrm{HFC}}$ and $P_{t,\mathrm{H_2}}^{\mathrm{MR}}$ are the amounts of hydrogen consumed by HFC and MR, respectively; α_{gh} is the green hydrogen certificate quota coefficient; $P_{t,\mathrm{H_2}}^{\mathrm{wind}}$ and $P_{t,\mathrm{H_2}}^{\mathrm{pv}}$ are the hydrogen production amounts from wind and photovoltaic power, respectively; and ω_{gh} is the quantification coefficient for converting hydrogen production amount into green hydrogen certificates.

If $Z_{\mathrm{GHCT}} > 0$, this indicates that the system needs to purchase green hydrogen certificate quotas from the hydrogen trading market. Conversely, the system can sell excess green hydrogen certificates to generate revenue. The cost of green hydrogen certificate trading can be expressed as:

$$F_{\mathrm{GHCT}} = \begin{cases} c_{\mathrm{GHCT}}\left(1+\delta_{\mathrm{gh}}\right)Z_{\mathrm{GHCT}} & -d < Z_{\mathrm{GHCT}} \le 0 \\ c_{\mathrm{GHCT}}Z_{\mathrm{GHCT}} & 0 < Z_{\mathrm{GHCT}} \le d \\ c_{\mathrm{GHCT}}\left(1+\mu_{\mathrm{gh}}\right)(Z_{\mathrm{GHCT}}-d)+\mu_{\mathrm{gh}}d & d < Z_{\mathrm{GHCT}} \le 2d \end{cases} \tag{9}$$

where λ_{GHCT} is the unit price of green hydrogen certificates; δ_{gh} and μ_{gh} are the reward and the penalty coefficients, respectively; and d is the range length of the green hydrogen certificate quota.

4. Model of Low Carbon Demand Response

4.1. Integrated Demand Response (IDR)

The electrical load response model is typically described using a price elasticity matrix, whereas thermal load has time delays and perception ambiguity, making it unsuitable for description using a price elasticity matrix. Instead, a first-order thermodynamic equation that reflects thermal load variation with temperature can be used to characterize it. Since the electrical and thermal load response models are extensively discussed in existing literature, this paper directly references the load response models from the reference [25] and focuses on the explanation of the LCDR mechanism.

4.2. Low Carbon Demand Response (LCDR)

The traditional IDR mechanism mainly focuses on system economics, optimizing the load curve by issuing price signals or incentive policies. However, it does not fully consider the low-carbon impact of load regulation. For the LCDR mechanism, it can be built on the traditional IDR mechanism by using carbon emission factors to enable the demand side to perceive the carbon emission levels of the supply side [26], allowing users to adjust their energy consumption strategies based on carbon emission intensity during different periods, thus achieving low-carbon dispatch on the demand side.

The carbon emissions to be allocated to the load side can be defined using the carbon emission factor as follows:

$$E_t^{\mathrm{load}} = E_t^{\mathrm{dir}} + E_t^{\mathrm{indir}} \tag{10}$$

$$\begin{cases} E_t^{\mathrm{dir}} = \sum\limits_i \max(\delta_{\mathrm{c},t}^{\mathrm{IES}} - \delta_{\mathrm{c},t}^{\mathrm{area}}, 0) \times (U_{i,t}^{\mathrm{total}} - U_{i,t}^{\mathrm{DR}}) \\ E_t^{\mathrm{indir}} = \sum\limits_i \max(\delta_{\mathrm{c},t}^{\mathrm{IES}} - \delta_{\mathrm{c},t}^{\mathrm{IES},0}, 0) \times U_{i,t}^{\mathrm{DR}} \end{cases} \tag{11}$$

where E_t^{load} is the total carbon emissions to be borne by the user side; E_t^{dir} and E_t^{indir} are the direct and indirect carbon emissions on the user side, respectively; $\delta_{\mathrm{c},t}^{\mathrm{area}}$, $\delta_{\mathrm{c},t}^{\mathrm{IES},0}$, and $\delta_{\mathrm{c},t}^{\mathrm{IES}}$ are the regional average carbon emission factor and the carbon emission factors before and after the user response, respectively; and $U_{i,t}^{\mathrm{total}}$ and $U_{i,t}^{\mathrm{DR}}$ are the initial load and the DR response of the user for the i-th category, respectively.

The interval carbon emission factor is issued by relevant authorities, while the carbon emission factors before and after the user response can be calculated as follows:

$$\delta_{c,t}^{IES} = (\delta_t^{c,e} P_{in,t}^{el} + \sum_n E_{n,t}) / (P_{in,t}^{el} + \sum_n P_{n,t}) \tag{12}$$

where $P_{in,t}^{el}$ is the total input power during the period; $\delta_t^{c,e}$ is the average carbon emission factor issued by the upper-level power grid; and $E_{n,t}$ and $P_{n,t}$ are the carbon emissions and output power during the operation of the n-th type of equipment, respectively.

When the demand side performs a low-carbon response, the following condition must be satisfied:

$$\begin{cases} 0 \le \Delta U_{t,i}^{+} \le U_{i,adj}^{max} \\ 0 \le \Delta U_{t,i}^{-} \le U_{i,adj}^{max} \\ U_{t,i}^{0} + \Delta U_{t,i}^{+} \le U_{t,i}^{N} \\ \left| \sum_{t=1}^{24} (\Delta U_{t,i}^{+} - \Delta U_{t,i}^{-}) \right| \le \Delta Q_i^{max} \end{cases} \tag{13}$$

where $\Delta U_{t,i}^{+}$ and $\Delta U_{t,i}^{-}$ are the increases and decreases in the i-th load under the LCDR mechanism, respectively; $U_{t,i}^{0}$ is the baseline load for the i-th category; $U_{i,adj}^{max}$ is the maximum adjustment capacity of the i-th load; $U_{t,i}^{N}$ is the maximum rated load for the i-th category; and ΔQ_i^{max} is the maximum change in the i-th load over a full day.

5. Opportunity Constrained Distribution Robust Model for IES

5.1. Opportunity Constrained Distribution Robustness Modeling

To fully account for the wind and solar forecasting errors and achieve flexible tunability of scheduling robustness, this paper constructed wind and solar forecasting error fuzzy sets based on the imprecise Dirichlet model theory and proposed a distributional robustness chance-constrained model.

5.1.1. Fuzzy Set of Wind and Solar Power Forecasting Errors

The IDM theory can accurately reflect the uncertainty of forecasting deviations and the probability of forecasting errors for renewable energy sources like wind and solar, while ensuring the robustness of the scheduling results [27]. Set the confidence level to α, then the real probability interval μ is constructed as follows:

$$\begin{cases} \mu^{-} = 0, \mu^{+} = f^{-1}\left(\frac{1+\alpha}{2}\right), & n_j = 0 \\ \mu^{-} = g^{-1}\left(\frac{1-\alpha}{2}\right), \mu^{+} = f^{-1}\left(\frac{1+\alpha}{2}\right), & 0 \le n_j \le N \\ \mu^{-} = g^{-1}\left(\frac{1-\alpha}{2}\right), \mu^{+} = 1, & n_j = N \end{cases} \tag{14}$$

where μ^{+} and μ^{-} are the upper and lower bounds, respectively, of μ; f and g are the cumulative distribution functions of the Beta distribution for μ^{+} and μ^{-}, respectively; and n_j and N are the sample size and the total sample size for the random variable ξ, respectively.

The fuzzy set of wind and solar forecasting errors can be represented as follows:

$$P = \left\{ G \in P_0\left(\left|\xi^{+}, \xi^{-}\right|\right) \middle| G[\xi \le \xi_m] \in [\mu_m^{+}, \mu_m^{-}],\ m = 1, 2, \cdots M \right\} \tag{15}$$

where $P_0(|\xi^{+}, \xi^{-}|)$ represents all probability sets within the range $[\xi \le \xi_m]$ and G is the cumulative probability distribution of the random variable ξ_m.

5.1.2. Distribution Robustness Opportunity Constrained Model

Based on the fuzzy sets, a distributional robustness chance-constrained model was constructed, providing upper and lower backup robust operating intervals to characterize the IES's tolerance for disturbances in renewable energy forecasting errors. When wind and solar forecasting errors are within the robust operating interval, the system's thermal power units can provide a spinning reserve for a rapid response. Conversely, if the errors exceed this interval, emergency measures such as wind curtailment, solar curtailment, or load shedding will be implemented to ensure the safe operation of the system. This paper, based on reference [28], constructed the joint probability distribution of wind and solar forecasting errors, and the distributional robustness chance-constrained model under this joint probability distribution is as follows:

$$\begin{cases} Q = \left\{ Q_t \in Q_t^*, Q_t^* = [-Q_t^-, Q_t^+] \right\} \\ P_r(-Q_t^- \le Q_t \le Q_t^+) = p_t^{\mathrm{up}} - p_t^{\mathrm{down}} \\ p_t^{\mathrm{up}} = F_{\mathrm{uni},t}^+(Q_t^+), p_t^{\mathrm{down}} = F_{\mathrm{uni},t}^-(Q_t^-) \\ 0 \le p_t^{\mathrm{up}} - p_t^{\mathrm{down}} \le 1 \\ \chi_t = p_t^{\mathrm{up}} - p_t^{\mathrm{down}} \\ Q_t^+ = r_t^{\mathrm{up}} / R_{\mathrm{uni}}, Q_t^- = r_t^{\mathrm{down}} / R_{\mathrm{uni}} \end{cases} \tag{16}$$

$$\begin{cases} P_{\mathrm{uni},t}^{\mathrm{curW}} = K_c \left(\int_{e_t^{\min}}^{Q_t^+} e_t dF_{\mathrm{uni},t}(e_t) \right) \\ P_{\mathrm{uni},t}^{\mathrm{curL}} = K_c \left(\int_{e_t^{\min}}^{Q_t^+} e_t dF_{\mathrm{uni},t}(e_t) \right) \\ \phi = \sum_{t=1}^{T} \chi_t \end{cases} \tag{17}$$

where Q_t and Q_t^* are the robust interval variables and the operating intervals, respectively; Q is the set of robust intervals; Q_t^+ and $-Q_t^-$ are the upper and lower bounds of the interval, respectively; p_t^{up} and p_t^{down} are the cumulative probabilities for the upper and lower bounds of the corresponding robust operating intervals, respectively; $F_{\mathrm{uni},t}^+$ and $F_{\mathrm{uni},t}^-$ are the upper and lower boundaries of the joint cumulative probability distribution of wind and solar forecasting errors, respectively; R_{uni} is the total installed capacity of wind and photovoltaic units; r_t^{up} and r_t^{down} are the upper and lower backup capacities provided by thermal power, respectively; χ_t is the robustness of the corresponding robust operating interval; $P_{\mathrm{uni},t}^{\mathrm{curW}}$ and $P_{\mathrm{uni},t}^{\mathrm{curL}}$ are the expected values of wind curtailment, solar curtailment, and load shedding risks outside the robust operating interval, respectively; ϕ is the robustness over one scheduling period; and e_t is the random variable of the joint forecasting error for wind and solar.

5.2. Multi-Objective Low-Carbon Robust Optimization Model

5.2.1. Economic Objective Function

The economic objective function aims to minimize the total operational cost of the system, considering the external procurement cost F_{Buy}, unit operation and maintenance cost F_{m}, wind and solar curtailment cost $F_{\mathrm{W,P}}$, green hydrogen certificate trading cost F_{GHCT}, thermal power operation cost F_{coal}, and spinning reserve cost F_{by}. The objective function is as follows:

$$\min F_{\mathrm{IES}}^{\mathrm{eco}} = F_{\mathrm{m}} + F_{\mathrm{Buy}} + F_{\mathrm{W,P}} + F_{\mathrm{GHCT}} + F_{\mathrm{coal}} + F_{\mathrm{by}} \tag{18}$$

(1) External Procurement Cost

The external procurement cost includes the electricity and gas purchase costs, represented as follows:

$$F_{\mathrm{Buy}} = \sum_{t=1}^{T} c_t^{\mathrm{e}} P_t^{\mathrm{Net,e}} + \sum_{t=1}^{T} c_t^{\mathrm{g}} \left(\frac{P_t^{\mathrm{HCHP,g}} + P_t^{\mathrm{HGB,g}}}{L_{\mathrm{g}}^{\mathrm{LHV}}} \right) \tag{19}$$

where c_t^{e} and c_t^{g} are the electricity and gas prices, respectively; $P_t^{\mathrm{Net,e}}$ is the electricity purchasing power; and $P_t^{\mathrm{HCHP,g}}$ and $P_t^{\mathrm{HGB,g}}$ are the gas consumption for HCHP and HGB, respectively.

(2) Operation and Maintenance Cost

$$F_{\mathrm{m}} = \sum_{t=1}^{T} \left(\sum_{n=1}^{N} \gamma_n P_t^n + \sum_{j=1}^{J} \pi_j (P_{t,j}^{\mathrm{c}} + P_{t,j}^{\mathrm{d}}) \right) \tag{20}$$

where N and J are the total number of energy conversion and storage devices, respectively; j is the type of storage device; $P_{t,j}^{\mathrm{c}}$ and $P_{t,j}^{\mathrm{d}}$ are the charging and discharging powers, respectively, of storage device j; and γ_n and π_j are the operation and maintenance coefficients, respectively, for device n and storage device j.

(3) Wind and Solar Curtailment Cost

$$F_{\mathrm{W,P}} = \sum_{t=1}^{T} \left(\varepsilon_{\mathrm{WT}} (P_t^{\mathrm{WT,0}} - P_t^{\mathrm{WT}}) + \varepsilon_{\mathrm{PV}} (P_t^{\mathrm{PV,0}} - P_t^{\mathrm{PV}}) \right) \tag{21}$$

where $P_t^{\mathrm{WT,0}}$ and P_t^{WT} are the wind power forecast and consumption power, respectively; $P_t^{\mathrm{PV,0}}$ and P_t^{PV} are the photovoltaic forecast and consumption power, respectively; and $\varepsilon_{\mathrm{WT}}$ and $\varepsilon_{\mathrm{PV}}$ are the wind and solar curtailment penalty cost coefficients, respectively.

(4) Thermal Power Operation Cost

The thermal power operation cost F_{coal} includes the coal consumption cost F_{mh} and the start-up and shutdown costs F_{qt}, and is expressed as:

$$F_{\mathrm{coal}} = F_{\mathrm{mh}} + F_{\mathrm{qt}} \tag{22}$$

$$\begin{cases} F_{\mathrm{mh}} = \alpha_k^{\mathrm{coal}} \sum\limits_{t=1}^{T} \sum\limits_{k}^{K} \left(a_k (P_{t,k}^{\mathrm{G}})^2 + b_k P_{t,k}^{\mathrm{G}} + c_k \right) \\ F_{\mathrm{qt}} = \sum\limits_{t=1}^{T} \sum\limits_{k=1}^{K} \left(U_{t,k}^{\mathrm{G}} (1 - U_{t-1,k}^{\mathrm{G}}) \delta_k^{\mathrm{G}} \right) \end{cases} \tag{23}$$

where K is the total number of thermal power units; $P_{\mathrm{G},k}^{t}$ and α_k^{coal} are the output power and unit coal consumption, respectively, cost coefficient for unit k; δ_{G}^{k} is the start-up and shutdown cost coefficient for unit k; $U_{\mathrm{G}}^{t,k}$ is the operating status of unit k; and a_k, b_k, and c_k are the coal consumption coefficients for unit k.

(5) Spinning Reserve Cost

$$F_{\mathrm{by}} = \sum_{t=1}^{T} \sum_{k=1} \left(c_k^{\mathrm{ur}} r_{t,k}^{\mathrm{up}} + c_k^{\mathrm{dr}} r_{t,k}^{\mathrm{down}} \right) \tag{24}$$

where c_k^{ur} and c_k^{dr} are the upper and lower reserve cost coefficients for unit k.

5.2.2. Low-Carbon Objective Function

The carbon emission sources of the IES in this paper come from thermal power units, purchased electricity (considered as coal-fired power plants), HCHP, and HGB, with the carbon emission calculation expressed as follows:

$$\begin{cases} D_{\text{coal}} = \sum_{t=1}^{T} \sum_{k=1}^{K} \left(x_k (P_{t,k}^{\text{G}})^2 + y_k P_{t,k}^{\text{G}} + z_k \right) \\ D_{\text{Grid}} = \sum_{t=1}^{T} \left(x_{\text{net}} (P_t^{\text{Net,e}})^2 + y_{\text{net}} P_t^{\text{Net,e}} + z_{\text{net}} \right) \\ D_{\text{total}}^{\text{gas}} = \sum_{t=1}^{T} \frac{44}{12} \lambda^{\text{CH}_4} \varphi^{\text{CH}_4} (\kappa_{\text{h-e}} P_{t,\text{e}}^{\text{HCHP}} + P_{t,\text{h}}^{\text{HGB}}) \\ D_{\text{MR}} = \sum_{t=1}^{T} \varphi_{\text{MR}} P_t^{\text{MR,g}} \end{cases} \tag{25}$$

The objective is to minimize the total carbon emissions of the system:

$$\min F_{\text{IES}}^{\text{low-c}} = D_{\text{coal}}^{\text{act}} + D_{\text{total}} + D_{\text{Grid}} - D_{\text{MR}} \tag{26}$$

where $F_{\text{IES}}^{\text{low-c}}$ is the total carbon emissions of the system; D_{coal}, D_{Grid}, and $D_{\text{total}}^{\text{gas}}$ are the carbon emissions from the thermal power units, purchased electricity, and HCHP, HGB, respectively; D_{MR} is the amount of CO_2 absorbed during the operation of MR; $\kappa_{\text{h-e}}$ is the electrical-thermal conversion factor; x_k, y_k, and z_k are the carbon emission calculation coefficients for unit k; x_{net}, y_{net} and z_{net} are the carbon emission calculation coefficients for purchased electricity; λ^{CH_4} and φ^{CH_4} are the carbon content rate and carbon oxidation rate, respectively, of natural gas per unit of thermal value; and $P_t^{\text{MR,g}}$ and φ_{MR} are the gas production power and CO_2 absorption efficiency of MR, respectively.

5.2.3. Robustness Objective Function

To balance the system robustness, robustness is incorporated as one of the optimization objectives to eliminate the subjective setting of system robustness. Since the compensation cost for load shedding is typically higher than the cost of wind and solar curtailment, it is necessary to increase the spinning reserve capacity to avoid load shedding. Based on Formulas (16) and (17), the robustness objective function can be established as follows:

$$\begin{cases} F_{\text{IES}}^{\text{Robust}} = \sum_{t=1}^{T} \left(p_t^{\text{up}} - \varphi^{\text{r}} p_t^{\text{down}} \right) \\ \varphi^{\text{r}} = \dfrac{\eta_1}{\eta_2} \end{cases} \tag{27}$$

where η_1 and η_2 are the penalty coefficients for load shedding and wind/solar curtailment, respectively; and φ^{r} is the reserve robustness importance coefficient.

5.3. Single Objective Processing of Multi-Objective Optimization

This paper is based on the Technique for Order Preference by Similarity to Ideal Solution (TOPSIS) method and multi-objective decision theory. It normalizes and optimally compromises three objective functions, transforming the multi-objective optimization problem into a single-objective optimization problem. The process is divided into the following three steps:

Step 1: To address the dimensional inconsistency issue in the IES objective functions, it is necessary to normalize the economic objective, low-carbon objective, and robustness objective:

$$\begin{cases} \boldsymbol{E} = [e_1, e_2, e_3] = [F_{\text{IES}}^{\text{eco}}, F_{\text{IES}}^{\text{low_c}}, F_{\text{IES}}^{\text{Robust}}] \\ h_i = \frac{e_i - e_i^{\min}}{e_i^{\max} - e_i^{\min}} \end{cases} \tag{28}$$

where h_i is the normalized value for the i-th objective; $\boldsymbol{E}$ is the vector form of the normalized objective function; e_i is the i-th objective of the system; and $e_i^{\max}$ and $e_i^{\min}$ are the minimum and maximum values, respectively, of e_i.

Step 2: Based on Formula (28), obtain the normalized optimal and worst solutions, and calculate the relative distance of the scheduling plan K to the optimal and worst solutions.

$$\begin{cases} D^+ = \sqrt{(h_1)^2 + (h_2)^2 + (h_3 - 1)^2} \\ D^- = \sqrt{(h_1 - 1)^2 + (h_2 - 1)^2 + (h_3)^2} \end{cases} \tag{29}$$

where D^+ and D^- are the relative distances of the scheduling plan to the optimal and worst solutions.

Step 3: The scheduling results obtained by the system are evaluated based on their proximity to the worst and optimal solutions. The multi-objective optimal trade-off function can be expressed as follows:

$$Y = \frac{D^-}{D^- + D^+} \tag{30}$$

where Y is defined as the trade-off optimization degree, with a range of $0 \leq Y \leq 1$; the closer Y is to 1, the better the scheduling result.

5.4. Constraints

The system constraints include equipment operation constraints, spinning reserve constraints, interaction power constraints, and power balance constraints. These have been extensively discussed in previous studies and will not be elaborated on here. For further details, refer to references [5,14].

5.5. Model Solution

The multi-objective optimal trade-off model constructed in this paper has high dimensionality and non-linearity. The IA-PSO algorithm is used to solve the proposed model, and its solution flowchart is shown in Figure 3.

The IA-PSO improvement method can be expressed as follows:

In traditional particle swarm optimization, the particle swarm only considers the current velocity, its own historical experience, and the historical best value. The particles are unable to determine whether this best value is the global optimum, which easily leads the swarm into local optima and premature convergence.

To address the issue of traditional particle swarm optimization easily falling into local optima, this paper introduces an adaptive inertia weight strategy and a dual-layer mutation operator based on the traditional particle swarm algorithm, proposing the IA-PSO algorithm. Firstly, an adaptive operator is introduced to adjust the inertia weight according to its fitness. Inertia weight A is a parameter in PSO that controls the extent to which the particle's previous velocity influences its current velocity. The adaptive inertia weight strategy dynamically adjusts A based on the particle's fitness or the number of iterations,

allowing it to focus more on local search capability to further optimize the current solution, as shown in Equation (31).

$$\varepsilon_0 = \varepsilon_{\min} + (\varepsilon_{\max} - \varepsilon_{\min}) \exp\left(\frac{1}{1 + (1 + \frac{k \cdot i}{i_{\max}})}\right) \tag{31}$$

where ε_0 is the current inertia weight; $\varepsilon_{\max}$ and $\varepsilon_{\min}$ are the maximum and minimum values of the inertia weight, respectively; k is the multiplication coefficient; and i and $i_{\max}$ are the current and maximum iteration numbers, respectively.

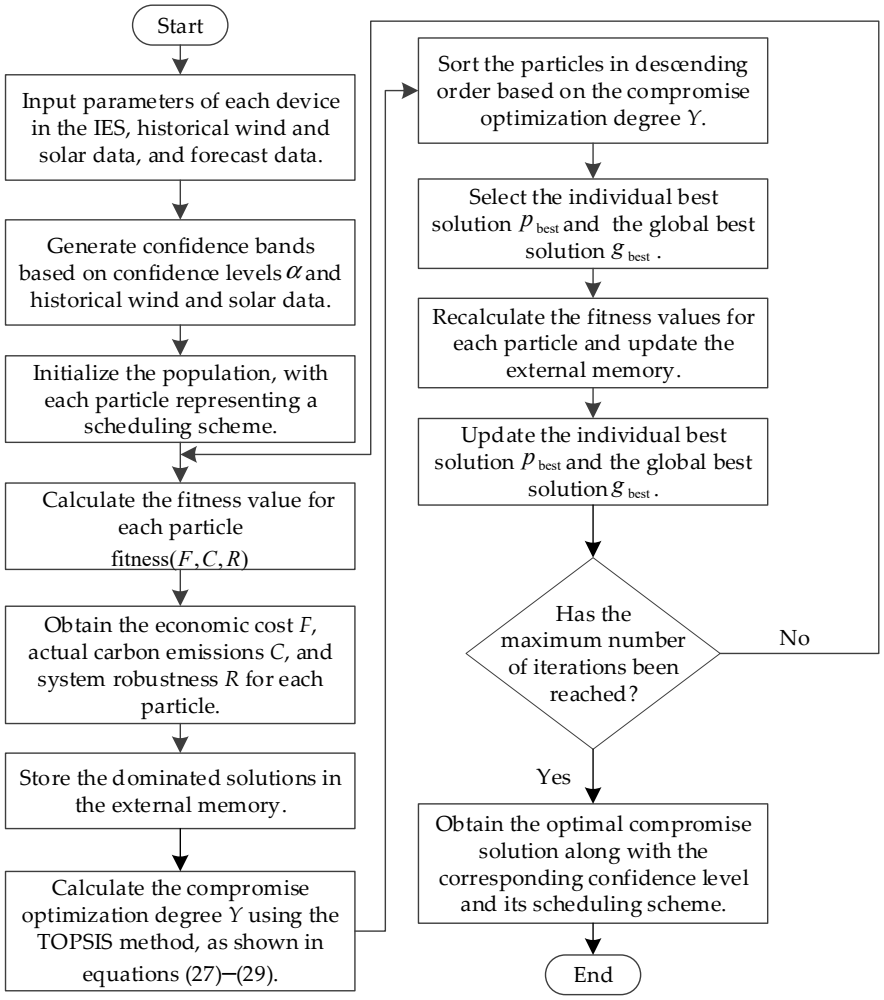


Figure 3. Algorithm solving flowchart.

Through this adaptive adjustment, the algorithm can balance the global and local search during the search process, encouraging particles to update their positions in an appropriate manner at different stages, thus gradually improving the overall fitness of the population and more effectively finding the optimal solution.

Based on Equation (31), a dual-layer mutation operator is further introduced. The first-layer operator adds a non-uniform mutation operator to perform the initial mutation operation during the particle swarm's search process. This mutation expands the search range of the swarm, enabling it to explore the entire search space more widely, as shown in Equation (32).

$$v_k' = \begin{cases} v_k + (v_{\max} - v_k) \cdot (1 - \text{rand}^{(1 - \frac{v_k}{T_{\max}})^b}) \\ v_k + (v_k - v_{\min}) \cdot (1 - \text{rand}^{(1 - \frac{v_k}{T_{\max}})^b}) \end{cases} \tag{32}$$

where T_{max} is the maximum iteration number and rand is a random number between [0, 1].

To avoid the algorithm getting trapped in local optima, the second mutation operator introduces the Cauchy mutation operator to mutate the optimal solution. This enhances the global search capability of the algorithm, helps the particle escape from local optima, prevents premature convergence, and improves the portability of the algorithm, as shown below:

$$\omega_k' = \omega_k \times \pi \tan(0.5 \times \text{rand} - 1) \exp\left(\frac{1}{1 + (1 + \frac{k \cdot i}{i_{max}})}\right) \quad (33)$$

where ω_k is the Cauchy distribution density function.

6. Case Study Analysis

6.1. Base Data

This paper takes the IES structure shown in Figure 1 as the subject. Since users' production and daily activities exhibit a clear daily cycle, such as industrial production typically occurring during the daytime on weekdays, and commercial and residential electricity consumption peaking in the evening, a 24 h scheduling cycle was adopted to accurately capture the peak and valley variations in load demand, facilitating the study of how to optimize energy scheduling to meet demand at different times and achieve a supply–demand balance. Additionally, actual power systems formulate generation plans one day in advance, and natural gas systems arrange the gas supply based on daily demand forecasts. Using a 24 h scheduling cycle for method validation provides a direct reference for actual scheduling plan development, making the research results more practical and actionable. Therefore, this paper conducted a case study analysis of the proposed model using a 24 h scheduling cycle.

The time-of-use electricity prices for IES were referenced from the reference [14]; Figure 4 shows the predicted curves for electricity and heat load, as well as renewable energy, derived from a real integrated energy park in the North China region; the parameters of the IES energy conversion devices and energy storage devices are presented in Tables 1 and 2 [5,14,24]; the operating parameters of the thermal power units are in Table 3 [4]; the penalty cost coefficients for wind and solar power curtailment are both 0.3; and the unit price for green hydrogen certificates is 200 RMB per certificate [11]. The confidence level was set at 95%. The parameters related to electricity and heat demand response were referenced from [24].

Table 1. IES device parameters. (In this table, ECE represents Energy conversion efficiency and O+M cost represents Operation and maintenance cost.).

Device	Rated Power/(MW)	ECE/%	Climbing Power/MW	O+M Cost/¥
HCHP	500	Electrical: 40 Heat: 50	100	0.056
HGB	900	90	200	0.03
AEL	350	92	50	0.025
HFC	250	88	40	0.015
MR	200	70	30	0.041

Table 2. IES energy storage equipment parameters. (In this table, C+DEC represents Charge and discharge energy constraints, ECE represents Energy conversion efficiency, and O+M cost represents Operation and maintenance cost.).

Device	Capacity/(MW)	C+DEC (MWh)	ECE/%	Climbing Power/%	O+M Cost/¥
BT	2000	200	95	20	0.015
TST	1500	150	92	20	0.045
HST	1500	150	92	20	0.022

Table 3. Equipment Parameters of Thermal Power Units.

Device	Rated Power/(MW)	Climbing Power/%	a/b/c (¥)
G1	250	20	0.0015/240/700
G2	250	20	0.0021/180/500
G3	200	20	0.0015/250/400

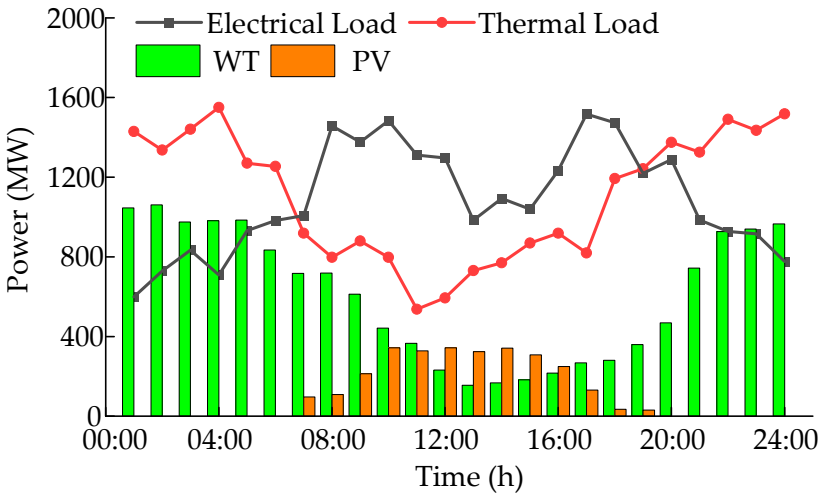


Figure 4. Electricity, Heat Load and Wind Power Prediction Curve.

6.2. Benefit Analysis

To verify the effectiveness of the proposed hydrogen IES scheduling model with green hydrogen trading and low-carbon demand response, the following scheduling schemes were compared.

Scheme 1: Traditional electricity-heat-gas IES scheduling model.

Scheme 2: Based on Scheme 1, an efficient hydrogen utilization model was introduced, consisting of AEL, HFC, MR, and hydrogen-doped gas components.

Scheme 3: Based on Scheme 2, the green hydrogen certificate trading mechanism was introduced.

Scheme 4: Based on Scheme 3, the traditional IDR strategy was introduced.

Scheme 5: Based on Scheme 3, the low-carbon IDR strategy was introduced.

All five verification schemes were analyzed based on a fixed system robustness (set to 21.58), with only economic efficiency as the optimization objective. Table 4 presents the cost comparison results under the five schemes.

Table 4. Optimization Results for Scheme 1 to 5. (In this table, PE cost represents Purchase electricity cost, PG cost represents Purchase gas cost, O+M cost represents Operation and maintenance cost, W+SC cost represents Wind and Solar Curtailment cost, and SR cost represents Spinning Reserve cost.).

Scheme	PE Cost/10^4¥	PG Cost/10^4¥	TPU Cost/10^4¥	O+M Cost/10^4¥	GHCT Cost/10^4¥	W+SC Cost/10^4¥	SR Cost/10^4¥	Total Cost/10^4¥	Carbon Emissions/t
1	35.88	206.26	158.64	75.69	/	40.83	45.36	562.66	9288.6
2	30.25	192.31	155.45	88.34	/	27.36	43.58	537.29	8322.7
3	32.66	189.25	154.48	88.37	−15.87	18.28	42.38	509.55	7669.4
4	24.43	184.39	148.37	84.39	−19.21	8.61	45.77	476.75	6922.7
5	22.19	181.27	143.14	86.55	−23.57	0	46.35	455.93	6457.3

6.2.1. Effectiveness Analysis of Efficient Hydrogen Utilization Link

To verify the effectiveness of the efficient hydrogen utilization components, Schemes 1 and 2 were compared. Figure 5 presents the results of efficient hydrogen utilization, and Figure 6 illustrates the electricity and heat scheduling balance results for Scheme 2. As shown in Figure 5, the large peak-valley difference in electricity and heat loads leads to the nighttime electricity load occurring at the valley and the heat load at the peak. Additionally, since the HCHP is influenced by the heat-to-electricity ratio, this results in higher wind power curtailment in Scheme 1. By combining the electricity and heat scheduling results from Figures 5 and 6, it is evident that Scheme 2 introduced efficient hydrogen utilization components, including hydrogen production, hydrogen-doped gas, hydrogen storage, and hydrogen use. The AEL operates during the periods of 01:00–08:00 and 18:00–24:00, converting surplus wind power into hydrogen at night. This hydrogen is then used to generate electricity and heat via the HFC, reducing the heating pressure during peak heating periods (01:00–06:00 and 19:00–24:00), and alleviating the wind power curtailment caused by the peak valley difference in electricity and heat loads. As shown in Figure 5, wind power consumption in Scheme 2 was significantly improved compared to Scheme 1. Additionally, the introduction of the hydrogen-doped gas component allowed the generated hydrogen to be fed into the gas pipeline for use by both HCHP and HGB, further improving the utilization pathways and efficiency of hydrogen energy.

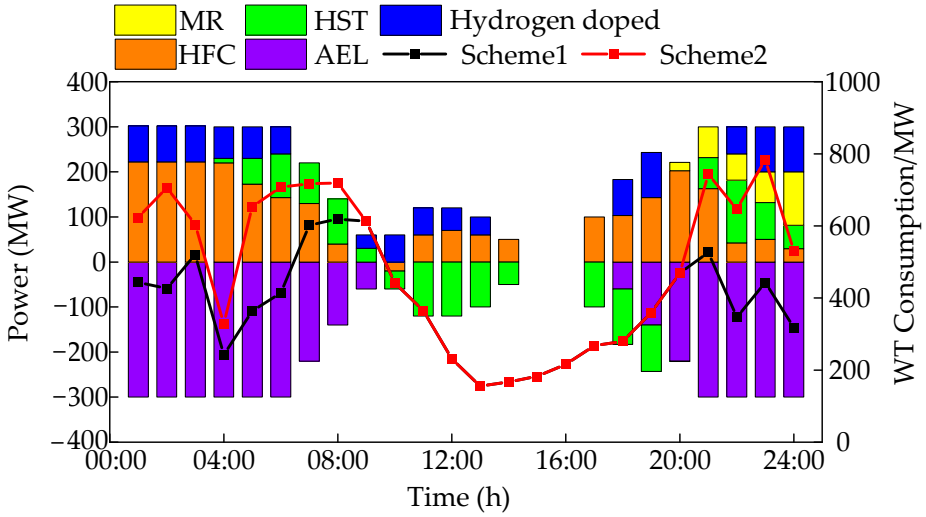
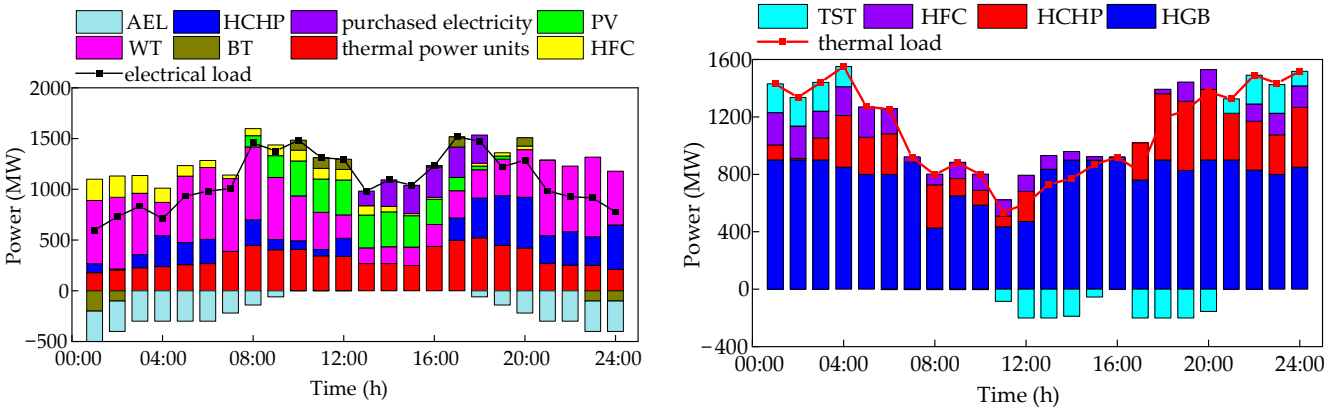


Figure 5. High efficiency hydrogen utilization results.



(**a**) Power energy scheduling results (**b**) Thermal energy scheduling results

Figure 6. The power and thermal energy scheduling results of Scheme 2.

According to Table 4, compared to Scheme 1, the wind and solar curtailment costs and the total IES cost in Scheme 2 decreased by 37.59% and 4.51%, while the total IES carbon emissions were reduced by 10.40%, confirming the effectiveness of the improved efficient hydrogen utilization model.

6.2.2. Effectiveness Analysis of Green Hydrogen Certificate Trading Mechanism

For Scheme 3, the green hydrogen certificate trading mechanism was introduced on top of Scheme 2. Figure 7 compares the green hydrogen ratios between Scheme 2 and Scheme 3. As shown in Figure 7, after introducing the green hydrogen certificate trading mechanism, Scheme 3 produced significantly more hydrogen compared to Scheme 2 during the nighttime periods when wind power is higher. Additionally, the green hydrogen ratio during the periods of 01:00–08:00 and 20:00–24:00 is 1, indicating that hydrogen production in these periods is entirely based on renewable energy. This not only improves renewable energy consumption but also reduces total carbon emissions. In contrast, for Scheme 2, the green hydrogen ratio was lower, and no hydrogen was produced during periods such as 11:00–17:00. According to Table 4, after introducing the green hydrogen certificate trading mechanism, Scheme 3 generated 158,700 yuan in green hydrogen certificate trading revenue. Compared to Scheme 2, its wind curtailment cost and total IES cost decreased by 33.19% and 5.16%, respectively, while total carbon emissions were reduced by 7.84%.

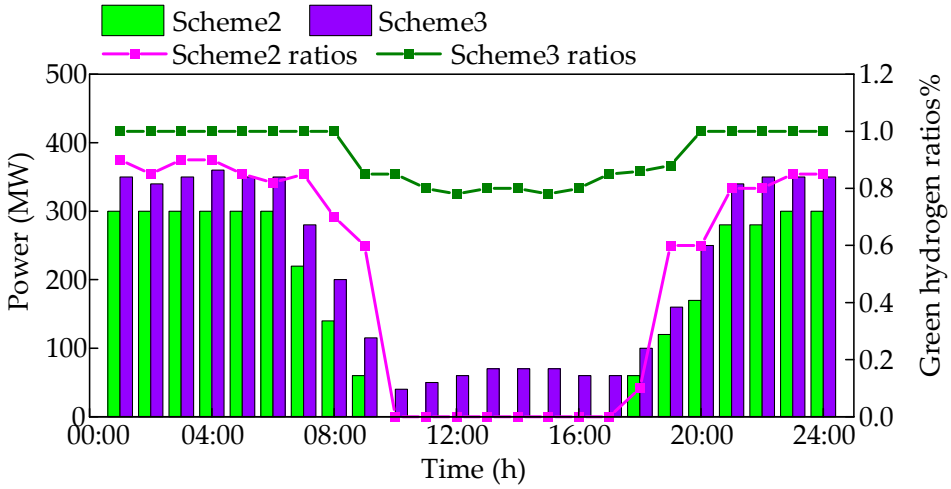
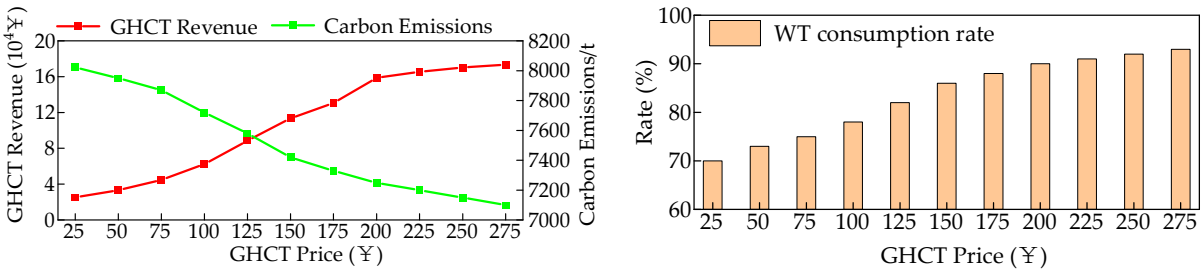


Figure 7. Comparison of the hydrogen production power and green hydrogen ratio results between Scheme 2 and Scheme 3.

Next, the impact of green hydrogen certificate trading prices on green hydrogen trading costs, carbon emissions, and wind power consumption is discussed, as shown in Figure 8. It can be observed that as the green hydrogen certificate trading price increased, both the green hydrogen certificate trading revenue and the wind power consumption rate for IES showed a continuous upward trend, initially rising rapidly and then gradually slowing down. This effectively incentivizes IES to adopt renewable energy-based hydrogen production. At the same time, the total carbon emissions of the system continued to decrease as the green hydrogen certificate trading price rose. Therefore, it can be concluded that after introducing the green hydrogen certificate trading mechanism, both the economic performance and low-carbon performance of IES are improved.

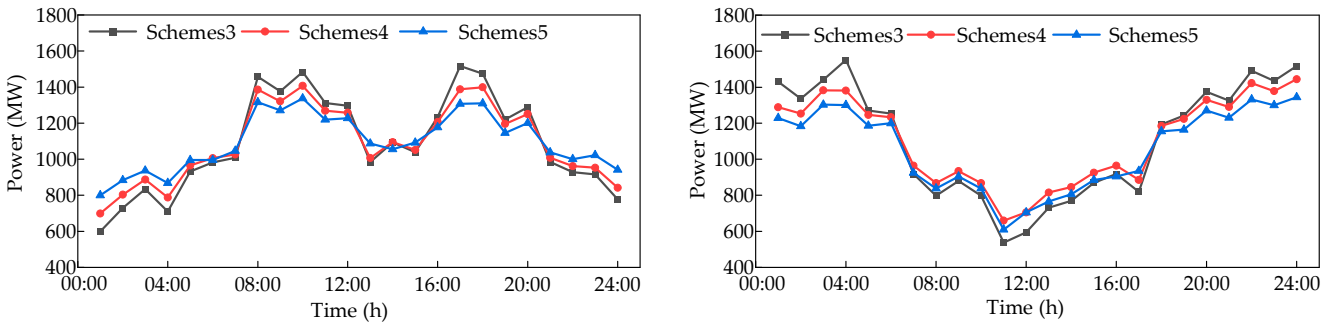


(**a**) (**b**)

Figure 8. The impact of green hydrogen certificate trading prices on the system. (**a**) The impact of CHCT price on CHCT revenue and Carbon Emissions. (**b**) The impact of CHCT price on WT consumption rate.

6.2.3. Effectiveness Analysis of Low-Carbon Demand-Response Strategy

Next, we compared Scheme 3 with Scheme 5. Figure 9 presents the optimization results of electricity and heat loads for Scheme 3 to Scheme 5. Scheme 3, due to the lack of demand-side response, exhibited a large peak-to-valley difference in both electricity and heat loads, resulting in significant wind curtailment and higher operational costs. In contrast, for Scheme 4, after introducing the electricity and heat IDR models, users can evaluate their energy costs based on time-of-use electricity prices and adjust their electricity consumption accordingly. Additionally, heat loads can be adjusted based on indoor and outdoor temperature changes. Both electricity and heat loads demonstrated peak shaving and valley filling trends, effectively reducing system operating costs and carbon emissions, while increasing wind power consumption during the night. Therefore, compared to Scheme 3, the wind and solar curtailment costs and total IES costs in Scheme 4 decreased by 52.90% and 6.44%.



(**a**) Optimization results of electrical load (**b**) Optimization results of thermal load

Figure 9. Optimization results of electrical and thermal loads for Schemes 3–5.

Scheme 5, which is based on Scheme 4, further introduced a low-carbon demand response, guiding the demand side to adjust energy consumption based on carbon emission factors. For electricity loads, since wind power is high at night, the carbon emission factor is low during this time. However, during electricity consumption peaks, such as 08:00–12:00 and 17:00–20:00, the carbon emission factor is higher due to the higher output power of coal-fired power plants. Therefore, after implementing the low-carbon demand response, users tend to shift electricity consumption from high-carbon periods to low-carbon periods, further enhancing the peak shaving and valley filling effect. For heat loads, since heating is primarily provided by gas-fired units, the carbon emission factor is low at night, reducing heating demand and alleviating the significant heating pressure during nighttime. During the day, however, due to a higher carbon emission factor, there is a slight reduction in heating demand. According to Table 4, compared to Scheme 4, the wind and solar curtailment costs in Scheme 5 dropped to zero, indicating that the renewable energy is fully consumed. Additionally, the total IES cost and carbon emissions decreased by 4.37% and 6.72%, respectively, verifying the effectiveness of the low-carbon demand-response strategy proposed in this paper.

6.3. Multi-Objective Optimal Trade-Off Analysis

6.3.1. Multi-Objective Collaborative Optimization Analysis

Schemes 1 to 5 were optimized solely for economic goals, with robustness set subjectively, resulting in relatively conservative scheduling schemes. To validate the effectiveness of the multi-objective collaborative optimization proposed in this paper, four additional schemes were set up for comparison based on Scheme 5′s scheduling scheme:

Scheme 6: considered economic and low-carbon collaborative optimization.

Scheme 7: considered economic and robustness collaborative optimization.

Scheme 8: considered low-carbon and robust-ness collaborative optimization.

Scheme 9: considered economic, low-carbon, and robustness collaborative optimization.

The optimization results of Schemes 5 to 9 are compared in Table 5, which presents the comparison of their economic, low-carbon, and robustness characteristics. As shown in Table 5, compared to Scheme 5, after considering economic and low-carbon collaborative optimization in Scheme 6, the total cost and carbon emissions decreased by 1.59% and 12.37%, respectively, significantly reducing the system's carbon emissions, thus demonstrating the low-carbon benefits of introducing the low-carbon goal. For Scheme 7, after considering economic and robustness collaborative optimization, compared to Scheme 5, the total cost and carbon emissions decreased by 3.23% and 6.73%, respectively, while robustness decreased by 3.29%. For Scheme 8, after considering low-carbon and robustness collaborative optimization, its carbon emissions and robustness decreased by 14.37% and 2.92%, respectively, while total costs increased by 4.90%. This indicates that by introducing the robustness objective, the issue of overly conservative IES operation decisions due to subjectively set robustness is avoided. For Scheme 9, by considering the collaboration of economic, low-carbon, and robustness objectives, its economic and low-carbon performance falls between those of Scheme 7 and Scheme 8, while its robustness improves by 2.78% and 2.53%, respectively, verifying the effectiveness of the collaboration of all three objectives.

The compromise optimization degree reflects how close the IES operating results are to the ideal virtual target. In terms of compromise optimization degree, Scheme 5 had the lowest compromise optimization degree, while Scheme 9′s compromise optimization degree improved by 17.43%, 12.06%, 6.98%, and 3.72% compared to Schemes 5 to 8, respectively. This demonstrated that multi-objective collaborative optimization results in scheduling schemes that are closer to the ideal virtual target than single-objective or dual-objective optimization, making the scheduling scheme more optimal.

Table 5. Comparison of different scheduling schemes.

Schemes	Total Cost/10^4¥	Carbon Emissions/t	Robustness Level	Compromise Optimization Degree
5	455.93	6457.3	21.58	0.522
6	448.67	5658.7	21.58	0.547
7	441.22	6022.5	20.87	0.573
8	478.25	5528.9	20.95	0.591
9	461.73	5811.4	21.45	0.613

6.3.2. Impact of Confidence Level on IES Operation

The confidence level reflects the likelihood of the probability distribution of wind and solar forecasting errors. The larger the confidence level, the more probability distributions are considered, which influences the system's scheduling results. In this paper, using a robustness level of 21.58 as an example, different confidence levels were set, and multi-objective optimal trade-off solutions were obtained to analyze the relationship between confidence levels, system spinning reserve capacity, and scheduling trade-off optimization degree.

As seen from Figure 10, with the increase in α, the system's compromise optimization degree decreased, and the spinning reserve capacity of the thermal power plants increased. This is because as α increased, the number of probability distributions included in the wind and solar forecasting errors increased. With the same spinning reserve, this resulted in a narrower robustness interval for the system, thus impacting the system's robustness benefits. Therefore, more spinning reserve capacity needs to be configured to achieve the same level of robustness, which increases the system's carbon emissions and operational costs. As shown in the figure, when α was 0.7, the system's compromise optimization degree was the lowest, and its corresponding carbon emissions, spinning reserve capacity, and total cost were the least. On the contrary, when α was 0.95, the system's carbon emissions, spinning reserve capacity, and total cost were the highest. Therefore, system decision-makers can select an appropriate confidence level according to actual needs to handle the impact of wind and solar forecasting errors on system operation.

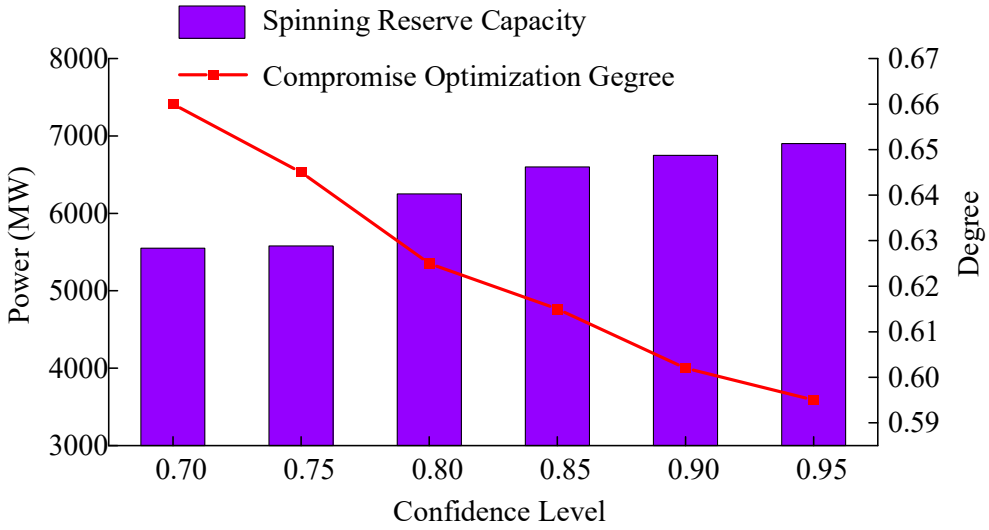


Figure 10. Results at different confidence levels.

6.3.3. Efficiency Analysis of Multi-Objective Optimal Trade-Off Model

This paper used IA-PSO and PSO, along with their multi-objective algorithms IA-MOPSO and MOPSO, to solve the multi-objective optimal trade-off scheduling model

and the multi-objective optimization scheduling model, respectively, and compared the results, as presented in Table 6. The population size and iteration count were both set to 100 and 400.

Table 6. Comparison of different scheduling strategies.

Model	Algorithm	Total Cost/10^4¥	Carbon Emissions/t	Robustness Level	Solution Time/s
The multi-objective optimal trade-off scheduling model	IA-PSO	461.73	5811.4	21.05	225
	PSO	465.28	6008.3	21.44	304
The multi-objective optimization model	IA-MOPSO	466.11	6063.8	20.79	856
	MOPSO	469.69	6187.3	21.14	1025

From the results in Table 6, it can be observed that when solving the multi-objective optimal trade-off scheduling model using IA-PSO and PSO, the solving efficiency of IA-PSO improved by 25.99% compared to PSO. Additionally, the IES total cost and carbon emissions decreased by 0.76% and 3.39%, respectively, verifying the advantages of the proposed solution algorithm. When comparing the multi-objective optimal trade-off model with the multi-objective optimization model, the former's solution time was 2.8 times shorter and 2.37 times faster than the latter. This is because the multi-objective optimal trade-off model does not require multi-objective optimal decision-making and successive non-inferior sorting during the optimization process, significantly reducing computational complexity and greatly improving the system's operational efficiency. Furthermore, as the multi-objective optimal trade-off model bypasses the Pareto optimal frontier, it directly obtains the optimal trade-off solution. Its IES total cost increased by 43,800 yuan and 44,100 yuan, and robustness improved by 1.25% and 1.42%, validating the effectiveness of the proposed multi-objective optimal trade-off model.

6.4. Simulation of Actual Case Example

To verify the effectiveness of the proposed model in real-world applications, this paper analyzed a practical integrated energy demonstration zone in Inner Mongolia, China. The system in this demonstration zone includes a thermal power plant with a total installed capacity of approximately 200 MW, consisting of three 100 MW thermal power units. The wind power installed capacity is approximately 450 MW, consisting of 90 units of 5 MW wind turbines; the solar power capacity is around 100 MW, with an additional 3 units of 100 MW combined heat and power units and 4 units of 150 MW gas boilers. Natural gas is sourced from the East Inner Mongolia region, and the water electrolysis hydrogen production system includes alkaline electrolyzers and hydrogen fuel cells. Additionally, an energy storage station and hydrogen storage system have been constructed. However, unlike the structure shown in Figure 1, this system does not include thermal storage tanks and methane reactors, which does not affect the validity of the proposed strategy in this study. This demonstration zone also includes a hydrogen refueling station primarily focused on hydrogen refueling for heavy-duty hydrogen-powered trucks, facilitating hydrogen consumption. Key parameters of the integrated energy demonstration zone equipment are shown in Tables 7 and 8, and the time-of-use electricity prices for the region are presented in Table 9. By integrating data from the energy management system and the data management platform of the demonstration zone, the electrical and thermal load data, as well as renewable energy generation data for 24 December 2024, at a 15 min time scale, were obtained, as shown in Figure 11.

Table 7. Conversion Equipment Parameters of the Demonstration Zone. (In this table, ECE represents Energy conversion efficiency and O+M cost represents Operation and maintenance cost).

Device	Rated Power/(MW)	ECE/%	Climbing Power/%	O+M Cost/¥
CHP	200	Electrical: 42.5 Heat: 49.3	20	0.056
GB	300	92	20	0.03
AEL	35	90.5	20	0.025
HFC	25	90	20	0.015

Table 8. Energy Storage Equipment Parameters of the Demonstration Zone. (In this table, C+DEC represents Charge and discharge energy constraints, ECE represents Energy conversion efficiency, and O+M cost represents Operation and maintenance cost.).

Device	Capacity/(MW)	C+DEC (MWh)	ECE/%	Climbing Power/%	O+M Cost/¥
BT	800	5	95	20	0.015
HST	50	5	92	20	0.022

Table 9. Electricity price parameters of IES.

Initial Electricity Price	Time Period	¥/kWh
Off-peak period	1:00–6:00, 23:00–24:00	0.385
Flat period	7:00–8:00, 13:00–17:00	0.555
Peak period	9:00–12:00, 18:00–22:00	0.888

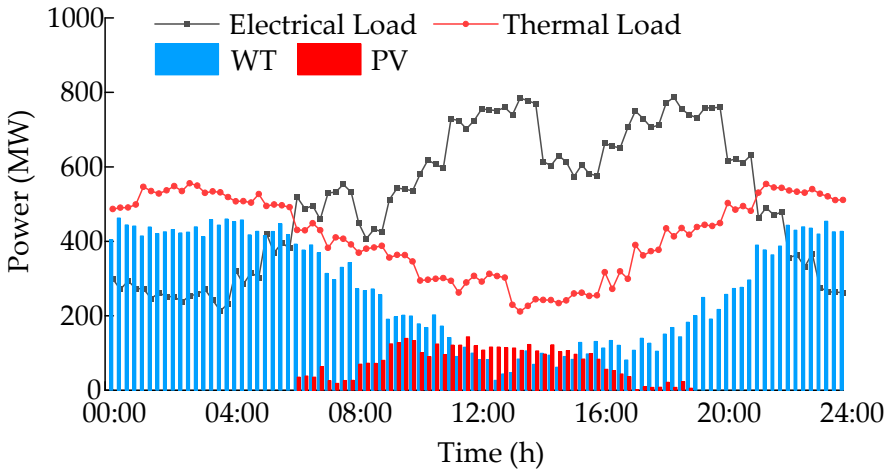


Figure 11. Load and Renewable Energy Forecast Data for the Demonstration Zone.

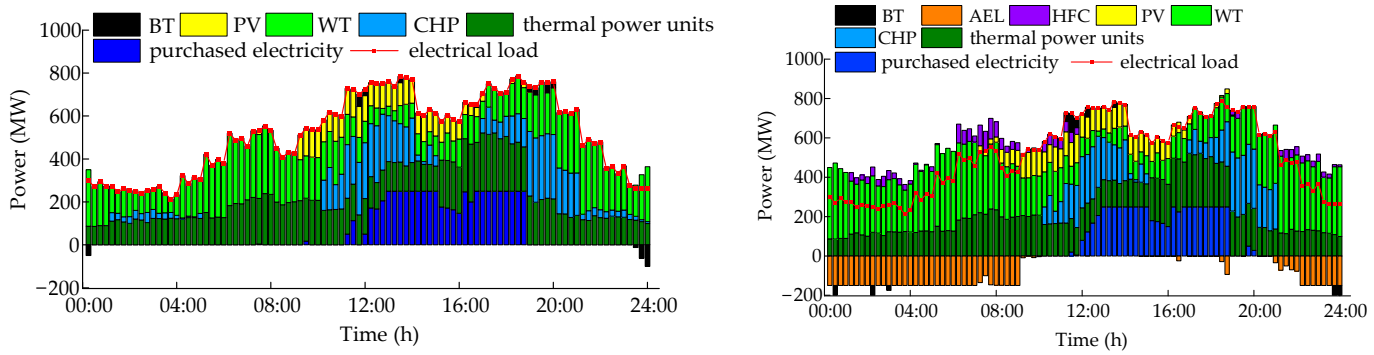
To verify the effectiveness of the proposed efficient hydrogen utilization, green hydrogen certificate trading mechanism, and low-carbon demand-response model, Schemes 1, 2, 3, and 5 from Section 6.2 were selected for validation. The resulting cost comparison is shown in Table 10.

Figure 12 shows the electricity comparison results between Scheme 1 and Scheme 2. As can be seen, after introducing the hydrogen utilization process in Scheme 2, AEL can convert wind power during periods such as 00:00–08:00 and 22:00–24:00 into hydrogen and then convert it into electrical and thermal power via HFC for use by the load side. As shown in Table 10, compared to Scheme 1, the wind power curtailment cost, total IES cost, and carbon emissions in Scheme 2 decreased by 34.82%, 4.45%, and 9.95%, respectively,

verifying the effectiveness of the efficient hydrogen utilization model. Similarly, Scheme 3, based on Scheme 2, further introduced the green hydrogen certificate trading mechanism, which generated a green hydrogen certificate trading revenue of 95,500 RMB for the system, further reducing wind power curtailment. As shown in Table 10, compared to Scheme 2, the total IES cost and carbon emissions in Scheme 3 decreased by 5.84% and 7.47%, respectively.

Table 10. Optimization Results of Scheme 1, Scheme 2, Scheme 3, and Scheme 5 (in this table, PE cost represents Purchase electricity cost, PG cost represents Purchase gas cost, O+M cost represents Operation and maintenance cost, W+SC cost represents Wind and Solar Curtailment cost, and SR cost represents Spinning Reserve cost.).

Scheme	PE Cost/10^4¥	PG Cost/10^4¥	TPU Cost/10^4¥	O+M Cost/10^4¥	GHCT Cost/10^4¥	W+SC Cost/10^4¥	SR Cost/10^4¥	Total Cost/10^4¥	Carbon Emissions/t
1	19.08	101.21	76.54	34.04	/	18.44	22.61	271.92	4623.14
2	16.40	94.57	75.02	40.06	/	12.02	21.75	259.82	4163.19
3	17.55	93.11	74.56	40.08	−9.55	7.70	21.18	244.63	3852.09
5	12.56	89.31	69.16	39.21	−13.22	0	23.07	220.09	3274.91



(**a**) Electricity scheduling results of Scheme 1 (**b**) Electricity scheduling results of Scheme 2

Figure 12. Comparison of Electricity Generation Between Scheme 1 and Scheme 2.

For Scheme 5, low-carbon demand response was introduced based on Scheme 3, guiding the demand side to adjust energy consumption based on carbon emission factors. Figure 13 shows the comparison results of the user-side electrical and thermal load responses before and after implementation. It can be seen that after introducing low-carbon demand response, both electrical and thermal loads exhibit varying degrees of peak shaving and valley filling, with results similar to those in Figure 9, effectively validating the effectiveness of the proposed strategy.

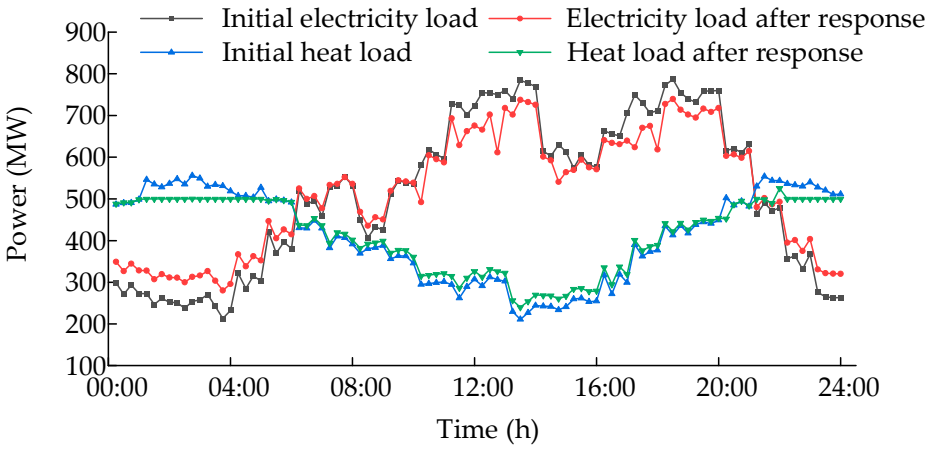


Figure 13. Load Response Results Before and After Low-Carbon Demand Response.

In summary, after using an actual integrated energy demonstration zone as the simulation case, the comparison results of Scheme 1 to Scheme 5 are consistent with the theoretical system trends, validating the effectiveness of the proposed efficient hydrogen utilization model, green hydrogen certificate trading mechanism, and low-carbon demand-response strategy in real system applications.

Similarly, to validate the effectiveness of the proposed multi-objective distributed robust optimization model in real systems, Schemes 5 to 9 from Section 6.3 were optimized, and the comparison results are shown in Table 11.

Table 11. Comparison of different scheduling schemes in Simulation of Actual Case Example.

Schemes	Total Cost/10^4¥	Carbon Emissions/t	Robustness Level	Compromise Optimization Degree
5	220.09	3274.9	20.88	0.504
6	215.86	2722.6	20.88	0.521
7	211.25	2988.4	19.74	0.545
8	238.24	2553.8	19.87	0.572
9	227.37	2746.9	20.45	0.598

As shown in Table 11, compared to Scheme 5, Scheme 6, after considering economic and low-carbon co-optimization, has reduced total cost and carbon emissions by 1.92% and 16.86%, respectively, significantly lowering the system's carbon emissions. For Scheme 7, after considering the co-optimization of economics and robustness, compared to Scheme 5, its total cost and carbon emissions decreased by 4.02% and 8.75%, while robustness decreased by 5.46%. For Scheme 8, after considering low-carbon and robustness co-optimization, its carbon emissions and robustness decreased by 22.02% and 4.84%, respectively, compared to Scheme 5, but the total cost increased by 12.77%. For Scheme 9, due to the co-optimization of economics, low-carbon, and robustness, its economic and low-carbon performance fell between those of Scheme 7 and Scheme 8, while its robustness improved by 3.59% and 2.77%, respectively, validating the effectiveness of the three-way co-optimization. From the perspective of compromise optimization, Scheme 5 had the lowest compromise optimization degree, while Scheme 9 had the optimal compromise optimization degree. In summary, the comparison trends of Schemes 5 to 9 are consistent with the theoretical system trends, which verifies the effectiveness of the proposed multi-objective distributed robust model in real system applications.

7. Conclusions

To address the issues of energy curtailment and uncertainty in IES with a high penetration of renewable energy, a multi-objective distributed robust low-carbon scheduling model for hydro-gen-enriched IES, incorporating green hydrogen trading and low-carbon demand response, was proposed. The following conclusions are drawn from the case study:

(1) The improved hydrogen utilization model can convert nighttime wind power into hydrogen through AEL and use hydrogen in various processes such as gas blending, HFC, and MR to convert it into electricity, heat, and gas. This not only significantly improves the absorption of nighttime wind power but also reduces the output of thermal power units in the system, thereby lowering carbon emissions. The results show that compared to the traditional electricity-heat-gas IES model, the introduction of the efficient hydrogen utilization model reduces the system's total cost by approximately 4.51% and carbon emissions by approximately 10.40%.

(2) The green hydrogen certificate trading mechanism effectively increases the amount of green hydrogen used in the system, reduces the proportion of hydrogen produced from coal power, and increases the level of renewable energy absorption. Under

the guidance of the green hydrogen certificate trading mechanism, the system can obtain green hydrogen trading revenue from the green hydrogen market, which not only reduces carbon emissions but also improves the system's economic performance. Furthermore, as the price of green hydrogen certificates increases, the green hydrogen certificate trading revenue and wind power absorption rate of the IES both show an upward trend, effectively encouraging IES to adopt renewable energy for hydrogen production. The results indicate that after introducing the green hydrogen certificate trading mechanism, the total cost and carbon emissions can be reduced by approximately 5.16% and 7.84%, respectively.

(3) Low-carbon demand response can guide the demand side to adjust its energy consumption based on carbon emission indicators by calculating the carbon emission factor for each time period. This effectively enhances the system's economy and low-carbon performance. Compared to the traditional demand-response model, the introduction of the low-carbon demand-response model further reduces the system's total cost and carbon emissions by approximately 4.37% and 6.72%.

(4) The proposed multi-objective optimal compromise model can transform a multi-objective optimization problem into a single-objective one. It not only considers the system's economy, low-carbon performance, and robustness simultaneously but also offers higher solution efficiency and optimization results compared to multi-objective optimization methods. The results show that after considering the optimal compromise treatment, the system's solution efficiency improves by 280% compared to multi-objective optimization methods.

In future research, the authors will introduce market trading mechanisms, focusing on the trading strategies among different stakeholders within the IES. They will propose an IES interaction model that considers multiple uncertainties and multi-agent games. Moreover, to ensure the practical application value of the proposed model, further numerical analysis will be conducted by integrating actual systems.

Author Contributions: Conceptualization, Y.Y. and H.Y.; methodology, Y.Y. and H.Y.; software, Y.Y. and H.Y.; validation, Y.Y., H.Y. and J.W.; formal analysis, Y.Y. and H.Y.; investigation, J.W.; resources, Y.Y.; data curation, H.Y.; writing—original draft preparation, H.Y.; writing—review and editing, Y.Y. and H.Y.; supervision, Y.Y. and H.Y.; project administration, Y.Y.; funding acquisition, Y.Y. All authors have read and agreed to the published version of the manuscript.

Funding: This research was funded by the Science and Technology Planning Project of Xinjiang Uygur Autonomous Region (2022A01007-3).

Data Availability Statement: All data are referenced in the article.

Conflicts of Interest: The authors declare no conflicts of interest.

Abbreviations

IES	Integrated Energy System	MR	Methane reactor
GHCT	Green Hydrogen Certificate Trading	PV	Photovoltaic
IDR	Integrated demand response	BT	Battery
LCDR	Low carbon demand response	HGB	Hydrogen-doped gas boiler
IA-PSO	Improving Adaptive Particle Swarm Optimization	HCHP	Hydrogen-doped combined heat and power
AEL	Alkaline Electrolyzer	TST	Thermal storage tank
HST	Hydrogen storage tank	IDM	Imprecise Dirichlet model
WT	Wind turbine	TOPSIS	Technique for order preference by similarity to ideal solution
HFC	Hydrogen fuel cell		

References

1. He, Z.; Liu, C.; Wang, Y.; Wang, X.; Man, Y. Optimal Operation of Wind-Solar-Thermal Collaborative Power System Considering Carbon Trading and Energy Storage. *Appl. Energy* **2023**, *352*, 121993. [CrossRef]
2. Shi, M.; Huang, Y. Dynamic Planning and Energy Management Strategy of Integrated Charging and Hydrogen Refueling at Highway Energy Supply Stations Considering on-Site Green Hydrogen Production. *Int. J. Hydrogen Energy* **2023**, *48*, 29835–29851. [CrossRef]
3. Rong, F.; Yu, Z.; Zhang, K.; Sun, J.; Wang, D. Performance Evaluation and Multi-Objective Optimization of Hydrogen-Based Integrated Energy Systems Driven by Renewable Energy Sources. *Energy* **2024**, *313*, 133698. [CrossRef]
4. Shahzad, S.; Alsenani, T.R.; Kilic, H.; Wheeler, P. Techno-Economic Analysis of Green Hydrogen Integration in Smart Grids: Pathways to Sustainable Energy Systems. *Int. J. Hydrogen Energy*, 2024; *in press*. [CrossRef]
5. Ge, S.; Zhang, C.; Wang, S. Optimal operation of integrated energy system considering multi-utilization of hydrogen energy and green certification-carbon joint trading. *Electr. Power Autom. Equip.* **2023**, *43*, 231–237.
6. Xia, J.; Zhang, Y.; Lei, H.; Liu, Z.; Chi, M. Low-Carbon Economic Dispatch of Integrated Energy System Considering Efficient Hydrogen Utilization and Carbon Capture Equipment. *Electr. Power Constr.* **2024**, *45*, 100–111.
7. Zhang, J.; Liu, Z. Low carbon economic scheduling model for a park integrated energy system considering inte-grated demand response, ladder-type carbon trading and fine utilization of hydrogen. *Energy* **2024**, *290*, 130311. [CrossRef]
8. Zhang, Z.; Chen, X.; Fu, Y.; Peng, X.; Li, Z. Distributionally Robust Low-Carbon Optimal Operation for Integrated Energy System Including Hydrogen Production from Off-shore Wind Power. *Power Syst. Technol.* **2025**, *49*, 41–51.
9. Liu, S. Research on Key Problems of Marketing of Hydrogen Production from New Energy Under the Background of Energy Transformation. Ph.D. Thesis, North China Electric Power University, Beijing, China, 2021.
10. Luo, Z.; Liu, D.; Jia, Y. Optimal operation of integrated energy system considering green hydrogen certificate and hydrogen production by hydropower. *Power Syst. Technol.* **2024**, *48*, 1445–1458.
11. Chen, M.; Chen, S.; Wang, Y.; Wei, N.; Pan, X. Chance constrained optimal scheduling of electric-hydrogen integrated energy system considering green certificate of hydrogen energy. *Electr. Power Autom. Equip.* **2023**, *43*, 206–213.
12. Yang, D.; Zuo, S.; Yang, J.; Sun, Y.; Li, B.; Liu, X. Low Carbon Economy Dispatch of Integrated Energy System Considering Green Hydrogen Certificate Trading Mechanism and Carbon Quota of New Energy Vehicles. *Power Syst. Technol.* **2025**, *49*, 562–571.
13. Wang, R.; Cheng, S.; Zuo, X.; Liu, Y. Optimal Management of Multi Stakeholder Integrated Energy System Considering Dual Incentive Demand Response and Carbon Trading Mechanism. *Int. J. Energy Res.* **2022**, *46*, 6246–6263. [CrossRef]
14. Li, Z.; Wang, Z.; Yao, Y.; Zhang, Z.; Deng, L. Low Carbon Operation of Hydrogen Energy Integrated Energy System Under Multitype Demand Response. *Proc. CSU-EPSA* **2024**, *36*, 44–54.
15. Chen, J.; Yang, K.; Zhang, Y.; Han, W.; Song, C. Optimal Scheduling of Integrated Energy System Considering Integrated Demand Response and Joint Operation of Carbon Capture and Power-to-Gas under Multiple Time Scales. *Electr. Power Autom. Equip.* **2024**, *44*, 68–76.
16. Cui, Y.; Wang, C.; Niu, Y.; Wang, K.; Yao, W.; Liu, C. Two-stage stochastic optimization decision of integrated energy system considering the uncertainty of integrated demand response. *Power Syst. Technol.* 2025; *accepted*. [CrossRef]
17. Yang, Z.; Xing, H.; Jiang, W.; Wang, H.; Sun, Y. Optimal scheduling of integrated energy system with coal-to-hydrogen and carbon capture power plant based on low-carbon demand response. *Electr. Power Autom. Equip.* **2024**, *44*, 25–32.
18. Gao, H.; Yin, B.; He, S.; Liu, J. A Distributionally Robust-Based Information Gap Decision Theory Optimization Method for Energy Station Considering Low-Carbon Demand Response. *Sustain. Energy Technol. Assess.* **2025**, *73*, 104129. [CrossRef]
19. Li, Y.; Wang, J.; Cao, Y. Multi-Objective Distributed Robust Cooperative Optimization Model of Multiple Integrated Energy Systems Considering Uncertainty of Renewable Energy and Participation of Electric Vehicles. *Sustain. Cities Soc.* **2024**, *104*, 105308. [CrossRef]
20. Wang, Y.; Qin, Y.; Ma, Z.; Wang, Y.; Li, Y. Operation Optimisation of Integrated Energy Systems Based on Cooperative Game with Hydrogen Energy Storage Systems. *Int. J. Hydrogen Energy* **2023**, *48*, 37335–37354. [CrossRef]
21. Fan, Y.; Liu, W.; Zhu, F.; Wang, S.; Yue, H.; Zeng, Y.; Xu, B.; Zhong, P.-A. Short-Term Stochastic Multi-Objective Optimization Scheduling of Wind-Solar-Hydro Hybrid System Considering Source-Load Uncertainties. *Appl. Energy* **2024**, *372*, 123781. [CrossRef]
22. Qin, P.; Tan, X.; Huang, Y.; Pan, M.; Ouyang, T. Two-Stage Robust Optimal Scheduling Framework Applied for Microgrids: Combined Energy Recovery and Forecast. *Renew. Energy* **2023**, *214*, 290–306. [CrossRef]
23. Wang, Z.; Han, Z.; Zhao, J.; Wang, W. Distributed Robust Scheduling Optimization for Energy System of Steel Industry Considering Prediction Uncertainties. *Inf. Sci.* **2024**, *666*, 120431. [CrossRef]
24. Shao, Z.; Lin, Y.; Chen, F. Distributionally robust low-carbon economic dispatch of electricity-gas-heat integrated energy system considering carbon-green certificate coupling mechanism. *Electr. Power Autom. Equip.* **2024**, *44*, 50–58+76.
25. Zhang, Z.; Fedorovich, K.S. Optimal Operation of Multi-Integrated Energy System Based on Multi-Level Nash Multi-Stage Robust. *Appl. Energy* **2024**, *358*, 122557. [CrossRef]

26. Zhang, C.; Wang, S.; Ge, S.; Pan, D.; Zhang, Y. Optimal Scheduling of Integrated Energy Systems Considering Flexible Demand Response and Carbon Emission-Green Certificate Joint Trading. *Electr. Power* **2024**, *57*, 14–25.
27. Cheng, Y.; Zhang, N.; Wang, Y.; Yang, J.; Kang, C.; Xia, Q. Modeling Carbon Emission Flow in Multiple Energy Systems. *IEEE Trans. Smart Grid* **2019**, *10*, 3562–3574. [CrossRef]
28. Zhang, H.; Chen, Y.; Wang, H.; Chang, X.; Zhao, M. Robust Fuzzy Dynamic Integrated Environmental Economic Dispatch for Multi-source System Considering the Double Uncertainty of Source-Load. *High Volt. Eng.* **2024**, *50*, 1446–1456.

Disclaimer/Publisher's Note: The statements, opinions and data contained in all publications are solely those of the individual author(s) and contributor(s) and not of MDPI and/or the editor(s). MDPI and/or the editor(s) disclaim responsibility for any injury to people or property resulting from any ideas, methods, instructions or products referred to in the content.